Transient analysis of the nonmonotonic response of counterflow laminar diffusion flames in alternating current and step electric fields using a one-dimensional ionic transport model

Byung Chul Choi [1],[*] and Pyeong Jun Park[2]

[1]*R&D Center, Korean Register of Shipping, Busan 46762, Republic of Korea*
[2]*School of Liberal Arts and Sciences, Korea National University of Transportation, Chungju 27469, Republic of Korea*

The electrohydrodynamic response of a counterflow laminar diffusion flame to applied alternating current (ac) electric fields is investigated experimentally and numerically. The flame positions are observed to show typical response to applied ac electric fields with high and moderate frequencies. The flame position does not respond above a threshold frequency corresponding to a certain collision response time, below which it oscillates in phase with the applied electric field. At a very low frequency (less than approximately 1 Hz), however, the flame position is observed to vary nonmonotonically as a function of time. To elucidate the nonmonotonic behaviors, a one-dimensional ionic transport model was employed by applying time-dependent electric fields. The responses of flame positions for ionized layers substituting for counterflow diffusion flames were systematically investigated with respect to one-way ionic wind (OIW) and two-way ionic wind (TIW) models. Consequently, it is demonstrated that the ionic models can produce not only harmonic flame oscillations for relatively low ac frequencies, but also free flame oscillations for stepwise voltages, which originated from the interaction between electrostatic force and ionic wind-induced force in the ionic system for both the OIW and TIW models.

I. INTRODUCTION

Electrohydrodynamic phenomenon has been widely applied in advanced thermal engineering including nonreacting and reacting flows; in particular, studies on the effects of electric fields on existing combustion systems are being actively conducted for the efficient use of fossil fuels with cleaner combustion [1,2]. The application of an electric field is known as one of the key technologies that can improve flame stabilization and reduce emissions [3–5]. Conversely, the oscillatory effects of electrohydrodynamic instability also occur in certain regions of the applied electric fields [6]. Thus, a deep understanding of this instability is essential to provide a stable energy transfer in combustors with electric fields. However, because of the abundance of charged ions and electrons produced by thermochemical reactions in a combustor, it is burdensome to deal with both the electrohydrodynamic forces exerted on charged matters by applied electric fields and the forces among those particles. Moreover, it is important to accurately describe collisions of neutral particles as well as collisions of charged particles. Thus, to approach the multiphysical problem efficiently, it is necessary to develop an appropriate model in which the convective bulk flow is modified under the effect of ionic or electric wind from momentum transfer [7,8].

In the reaction zone of a hydrocarbon flame, positively charged species such as H_3O^+, $C_3H_3^+$, CH_3^+, and CHO^+ have number densities of the order of 10^9 to 10^{11} ions/cm^3

[9,10]. They are driven by external electric fields and transfer their momentum to neutral molecules by collision [7]. Therefore, single-charged positive ions can be considered primarily for momentum balance [6,11] by assuming the contribution of anions and electrons to be relatively small [7]. In addition, negatively charged species such as OH^-, O^-, $C_xH_y^-$ hydrocarbon ions, $C_xH_yO_z^-$ oxygen-containing ions, and electron-attached O_2^-, H_2O^- exist on the order of 10^{10} ions/cm^3 [9,12,13]. They are driven by external electric fields and interact in the opposite direction of the moving positive ions with respect to the applied ac and dc electric fields. The ionic wind effect caused by both the positive and negative ions in several flow configurations has been investigated using numerical calculations [14–18] and experimental visualization [19,20].

Electrons can play crucial roles for electron attachment [21], dissociative attachment [22], and direct momentum transfer to neutrals [23]. Therefore, although they are lighter and smaller than charged and neutral molecules, the direct and indirect interactions of the electrons produced in the reaction zone can be significant in the ionic wind effect, owing to their higher mobility and larger diffusion coefficient [24,25]. In our previous study [25], incorporating the electric force acting on the electron together with the effect of charged ions, a one-dimensional (1D) ionic transport model has been proposed and compared by applying the own-way (unidirectional) and two-way (bidirectional) ionic wind models. The results emphasized that the nonlinear responses of a counterflow diffusion flame in the applied dc electric fields could be classified into a one-way ionic wind (OIW)-dominated regime for relatively low dc voltages, two-way ionic wind

*byungchul.choi@hotmail.com

(TIW)-induced regime for relatively high dc voltages, and the transition regime between the two regimes. However, unstable behaviors of flame positions under a certain range of the applied dc voltages remained an unsolved problem.

The interesting phenomenon of time-varying unstable flame positions has been rarely reported, despite the constant applied dc electric fields. In a similar study, the electro-hydrodynamic instability of a premixed stagnation flame was observed at approximately $V_{dc} = 1.5$ kV and analyzed quantitatively using the experimental method of particle image velocimetry and CH* chemiluminescence, by comparing with two-dimensional simulations [26]. Flame oscillation was observed at the transition to saturation ion current at approximately $V_{dc} = 1.2$kV in a coflowing nonpremixed methane/air flame and analyzed using transient CH* chemiluminescence and ion current signals [27]. Under a fixed propane–butane flow rate and a constant potential difference, the free-oscillation regime for the diffusion flame was observed at approximately the order of $V_{dc} = 1$ kV in the interelectrode gap and analyzed using the radiation strengths of CH^* and C_{2*} radicals and the current between the electrodes [28]. The underlying mechanism regarding the nontrivial flame oscillation in a constant electric field is still to be uncovered.

Although the counterflow diffusion flame has been numerically conducted in depth by applying dc electric fields [29,30], studies on unsteady flame behavior in ac electric fields with relatively low frequencies are still limited. In this study, the dynamical position of methane diffusion flame diluted with nitrogen in a counterflow burner is examined experimentally by applying ac electric fields. To illustrate the oscillations of the flame positions, the effects of time-varying electric fields with a sine function on the flame positions were numerically investigated using the 1D ionic transport model and analyzed by comparing the OIW and TIW effects. In particular, to understand the nonmonotonic behavior that occurs peculiarly in ac electric fields of relatively low frequencies in the order of 0.1 Hz, unsteady flame positions were analyzed by applying stepwise dc electric fields.

II. EXPERIMENTAL SETUP

The experimental apparatus used in this study was identical to that used in the previous study [25], except that ac electric fields were applied instead of dc electric fields. The main components comprising a counterflow burner, flow controllers, an electric power supply, and a visualization setup are shown in Fig. 1. The counterflow burner had two divergent-convergent nozzles with an area ratio of 36:1 to obtain a near-uniform velocity profile. Fuel and oxidizer were supplied in opposite directions through nozzles of inner diameter 1.0 cm to form a counterflow diffusion flame. The distance between the two nozzles was fixed at 1.6 cm. The fuel was a mixture of chemically pure-grade methane ($> 99.98\%$) and nitrogen diluent ($> 99.99\%$). The fuel mole fraction was set to $X_{F,0} = 0.3$ to suppress soot formation. The oxidizer was a mixture of 21% oxygen ($> 99.99\%$) and 79% nitrogen. Both nozzle exit velocities were set to 30 cm/s (stretch rate ≈ 72 s^{-1} [20]). To prevent flow disturbance, shielding nitrogen was supplied through concentric slits of inner diameter 1.2 cm at the outer sections of the fuel and oxidizer exits. The flow rates of the
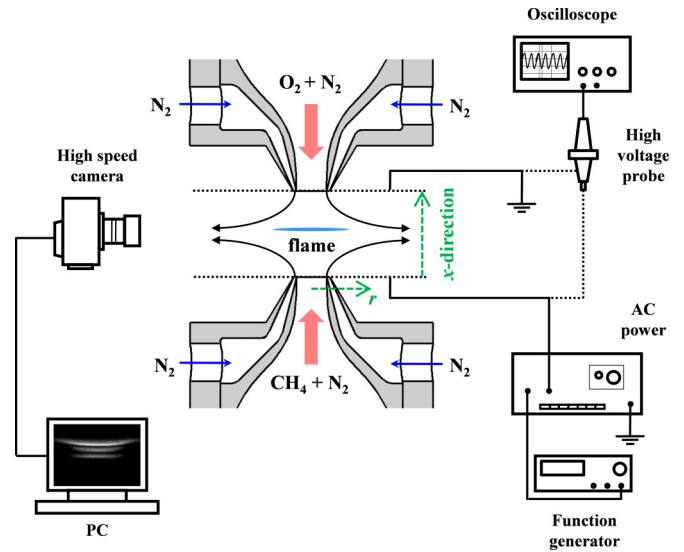
FIG. 1. Schematic diagram of experimental setup.

fuel and oxidizer were controlled by mass flow controllers calibrated with a wet gas meter.

An electric power supplier (Trek, 10/10B-FG) and a function generator (NF, WF1943B) were used to apply the ac voltage as root-mean-squared values. The ac voltage output from the electric power supplier was connected to one of the circular meshes of diameter 60 mm placed at the lower nozzle exit of the fuel side. The other meshes placed at the upper nozzle exit of the oxidizer side and the ground terminal from the electric power supply were connected to the building ground to maintain reasonably uniform electric fields between the fuel and oxidizer exits. The voltage profile was monitored using an oscilloscope (Tektronics, TDS 1012B) and a 1000:1 voltage divider (Tektronics, P6015A). The flame images were captured using a high-speed camera (Photron, Fastcam Ultima 1024) at a maximum shutter speed of 500 fps. The responses of the diffusion flame with respect to the applied ac electric fields were monitored and represented by the flame position x_f along the centerline of $y = 0$, which was defined as the location of maximum luminosity.

It is noted that the self-similarity assumption typically allows the quasi-1D governing equations and analysis along the axis of symmetry for the counterflow burner [31]. Specifically, the centerline profiles of two-dimensional (2D) axisymmetric counterflow burners were investigated by Johnson *et al.* [32] concerning the aspect ratios of $0.67 < 2R/L < 2.6$. The results showed that the differences in physical profiles along the centerline were greater than those of the larger aspect ratio (a Seshadri-type burner of $2R = 26$ mm) by comparing with the numerical quasi-1D solutions. This suggested a suitable aspect ratio for the purpose of the quantitative experiment for validation of numerical simulations. Although the insufficiently slender burners have quantitatively less compatibility with the self-similarity assumptions, the results of the counterflow experiments with the geometrical conditions of $2R/L = 0.67$ and 1 indicated a comparable trend in the flame positions on the centerline and current density under the stoichiometric mixture fractions of $Z_{st} = 0.07$ and 0.5 in the case of dc
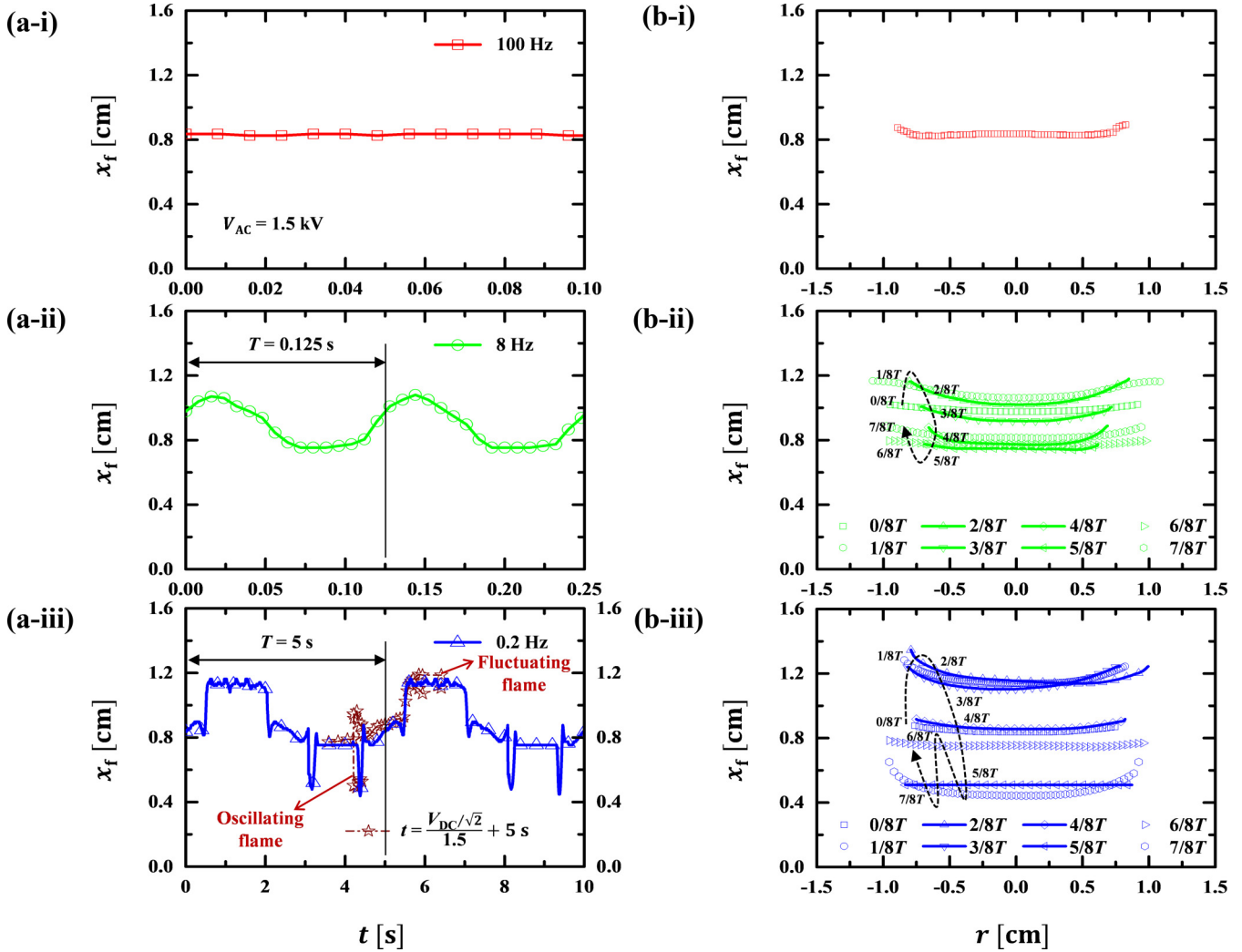
FIG. 2. Representative responses of (a) central flame position including dc data [25] and (b) radial flame profile with time.

electric fields [20]. For ac electric fields, furthermore, the amplitudes of flame oscillations responding to the time-varying applied voltages were identically characterized using both the aspect ratios of $2R/L = 0.5$ and 1 under the stoichiometric mixture fraction of $Z_{st} = 0.5$ [33]. In this regard, we selected a geometrical condition with the aspect ratio of $2R/L = 0.625$ and a stoichiometric mixture fraction of $Z_{st} = 0.228$ in the present experiment. The main purpose of this study was to analyze the dynamic variations in the flame positions along the centerline by applying the external electric fields.

III. EXPERIMENTAL RESULTS AND DISCUSSION

Figure 2 shows the flame position x_f with respect to the time (a) and radial profile of the flame positions corresponding to each period (b), which was divided into eight pieces ($0/8T$–$7/8T$), when an ac voltage of $V_{ac} = 1.5$ kV was applied to the counterflow diffusion flame by varying the representative ac frequency of (a) $f_{ac} = 100$ Hz, (b) 8 Hz, and (c) 0.2 Hz. For (a) $f_{ac} = 100$ Hz as a high frequency, the flame position (a-i) was almost constant at $x_f = 0.83$ cm with slight deviations of $\pm 1.8\%$. The radial flame profile (b-i) was almost stationary and axisymmetric. This was

consistent with the previous result that the maximum threshold frequency having no distinctive movement of flame position was approximately 35 Hz [34] corresponding to the collision response time of approximately 14 ms [35–37], regardless of the increase in the applied ac voltage.

For (b) $f_{ac} = 8$ Hz as an intermediate frequency, the flame position (a-ii) oscillated sinusoidally with a period of $T = 0.125$ s. The oscillation amplitude was approximately 0.33 cm for the maximum and minimum values of $x_f = 1.08$ and 0.75 cm, respectively. The radial flame profile (b-ii) exhibited a longer length when rising (marked as symbols) compared with when falling downward (marked as solid lines with symbols). The typical behavior of the flame positions responding to ac voltages with relatively high frequencies was consistent with previous experimental results [33,34].

For (c) $f_{ac} = 0.2$ Hz as a low frequency, the flame position in Fig. 2(a-iii) shows a complex response with rising and falling patterns compared with the sinusoidal oscillation shown in Fig. 2(a-ii). As time progressed, the flame position jumped up rapidly from the halfway location to the upper oxidizer side and exhibited a fluctuating motion. Subsequently, the flame position repassed the halfway location and exhibited a momentary falling-down motion with two sharp points at

the lower fuel side. The radial flame profiles in Fig. 2(b-iii) showed generally similar shapes with those of Fig. 2(b-ii) while the radial profiles tended to be slightly tilted around the upper oxidizer nozzle. This nonmonotonic behavior of the flame position closely resembles the nonlinear response of the flame positions as a function of the applied dc voltage [25]. Previous data of flame positions for applying dc electric fields in the same experimental configuration was rescaled to RMS ac voltages with the time and replotted for a period as star symbols in Fig. 2(a-iii). When a positive dc voltage of $V_{dc} = +2$ kV was applied to the lower fuel side, the flame position was shifted toward the upper oxidizer side connected to the ground and exhibited some fluctuations with the maximum and minimum values of $x_f = 1.19$ and 1.07 cm, respectively. Meanwhile, the flame position under the opposite polarity of $V_{dc} = -1.5$ kV moved toward the lower fuel side and oscillated periodically at a frequency of approximately 5 Hz. The oscillation amplitude was approximately 0.51 cm for the maximum and minimum values of $x_f = 0.99$ and 0.48 cm, respectively.

It is interesting to compare the dynamic behavior of the flame position with respect to time between dc and ac electric fields. As shown in Fig. 2(a-iii), the fluctuating flame motion in dc electric fields reappeared during the time interval in which the flame positions were located in the upper direction by the slowly varying ac electric fields. Furthermore, the oscillating flame motion in dc electric fields reappeared during the time interval in which the flame positions were located in the lower direction by the slowly varying ac electric fields. This implies that the nonmonotonic behavior of the flame position considered as electrohydrodynamic instability can be understood by adopting a comparative methodology of the constant and slowly varying the voltages in terms of time. The following section provides detailed discussions.

Figure 3 shows the flame positions as a function of time for the representative ac voltage and frequency, except for the range of relatively high frequency. In Fig. 3(a) $f_{ac} = 12$ Hz, the amplitudes of the flame oscillation became larger as the applied ac voltage increased to $V_{ac} = 0.8$, 2.0, and 7.0 kV. In Fig. 3(c), $f_{ac} = 0.2$ Hz. Here, although the response of the flame position in the case of $V_{ac} = 2.0$ kV exhibited a momentary falling-down motion in the lower fuel side, which was similar to that of $V_{ac} = 1.5$ kV as shown in Fig. 2(a-iii), the rapid flame motion did not appear and was unclear for $V_{ac} = 0.8$ and 7.0 kV. Meanwhile, the time interval in which the flame fluctuation occurred in the upper oxidizer side was further expanded as the applied ac voltage increased. In Fig. 3(b) $f_{ac} = 2$ Hz, the transition behavior between those of (a) $f_{ac} = 12$ and (c) 0.2 Hz is exhibited.

The significant changes in the flame position with respect to the representative combinations of V_{ac} and f_{ac} can be categorized into three regions: (1) the stable behavior in the relatively high frequency of $f_{ac} \approx 100$ Hz, (2) the sinusoidally oscillating behavior in the intermediate frequency of $f_{ac} \approx 10$ Hz, and (3) the nonmonotonically oscillating behavior in the relatively low frequency of $f_{ac} < 1$ Hz. To understand the underlying mechanism that results in nonmonotonic flame responses with respect to time, a numerical study was performed for a qualitative comparison between the OIW and TIW wind effects in the next section.
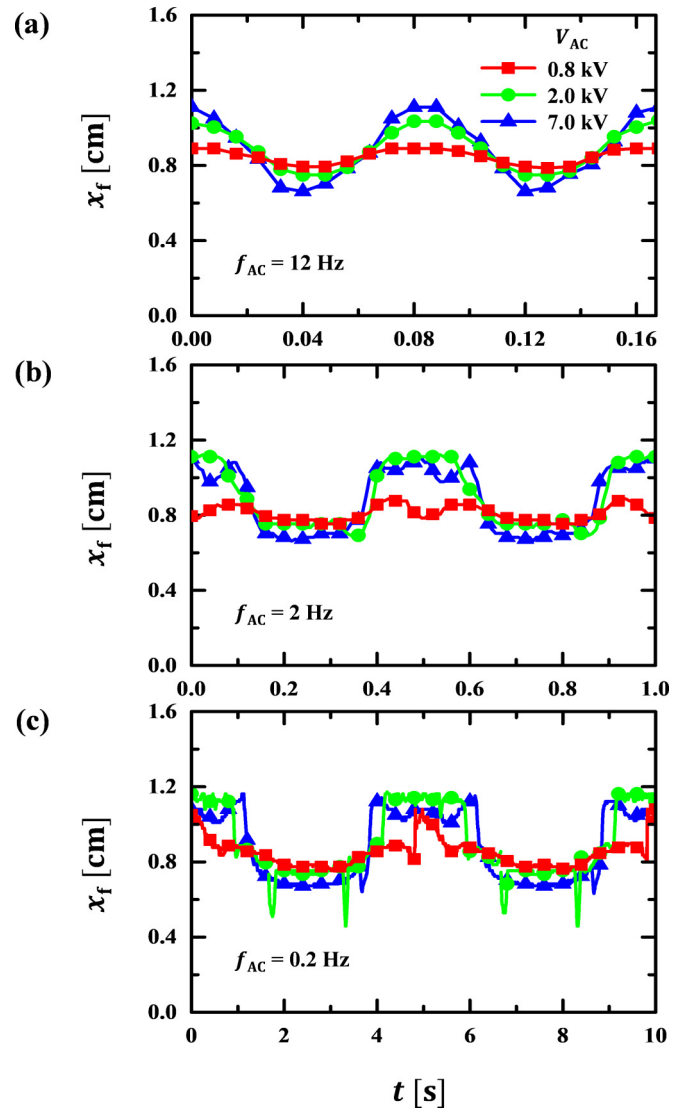
FIG. 3. Dynamic flame positions for the representative ac voltage and frequency.

On the other hand, the nonsymmetrical flame shapes appeared instantaneously as shown in Fig. 2(b-iii) and the difference in the flame positions between the upper and lower directions shifted by the electrohydrodynamic force appeared obviously as shown in Fig. 3(c). These may be affected by not only the initial flame position due to species diffusion, but also the buoyancy exerted by a chemical reaction in the three-dimensional counterflow structure, but are neglected in the present study. The governing equations such as mass, momentum, energy, and species conservations including a detailed kinetic mechanism and a state equation of ideal gas must be considered to advance the quantitative analysis in the future. Nevertheless, the following 1D ionic transport model can be useful to provide physically important insights.

IV. ONE-DIMENSIONAL IONIC TRANSPORT MODEL

As reported in the previous study regarding dc electric fields, the time evolutions of number densities have
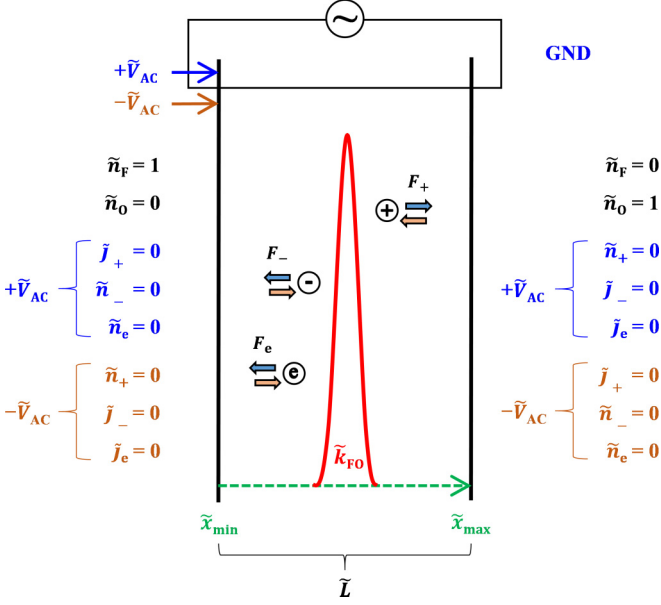
FIG. 4. Schematic diagram of numerical model.

been suggested as a 1D simple model based on convection-diffusion-reaction equations [25]. The number densities of $n_i(x, t)$ are defined as a function of position x and time t, where the subscript i represents the fuel, oxygen, or charged species k. Subsequently, the coupled nonlinear system response to dc electric fields was solved as a steady-state equation by $\frac{\partial n_i}{\partial t} = 0$. In the present study regarding ac electric fields, the distributions of number densities in the 1D ionic transport model evolved in time by numerical integration, i.e., $n_i = n_{i,0} + \int \frac{dn_i}{dt} \, dt$, where $n_{i,0}$ is the initial profile of $n_i(x, 0)$ with no electric field.

When applying ac electric fields, the schematics of the 1D ionic transport model for the fuel side at $x_{min}(x = 0)$ and at the oxygen side at $x_{max}(x = L)$ in an x coordinate are expressed in a dimensionless quantity, as shown in Fig. 4. The constant boundary conditions for $n_F(x, t)$ and $n_O(x, t)$ are specified as follows:

$$n_F(0, t) = n_{F,0}, \tag{1}$$

$$n_F(L, t) = 0, \tag{2}$$

$$n_O(0, t) = 0, \tag{3}$$

$$n_O(L, t) = n_{O,0}, \tag{4}$$

where $n_{F,0}$ and $n_{O,0}$ are the initial number densities of fuel and oxygen at the nozzle exits, respectively. The time-varying sinusoidal electric potential differences between the boundary conditions are defined as

$$V(0, t) = V_{ac} \sin(2\pi f_{ac} t), \tag{5}$$

$$V(L, t) = 0, \tag{6}$$

where the applied ac voltage of $V(x, t)$ periodically reverses direction with respect to the peak voltage V_{ac} and frequency

f_{ac}. As the polarity of the applied voltage changes, the boundary conditions for charged species k are reversed. When a positive ac voltage $[V(0, t) > 0]$ is applied in the $+x$ direction and $x = x_{min}$, the positive ions are reflected and the negative ions and electrons are absorbed at the fuel side, as expressed in Eq. (7). When $x = x_{max}$, the positive ions are absorbed and the negative ions and electrons are reflected at the oxygen side, as expressed in Eq. (8):

$$\{j_+(0, t), n_-(0, t), n_e(0, t)\} = 0 \qquad \text{for } x = x_{min}, \tag{7}$$

$$\{n_+(L, t), j_-(L, t), j_e(L, t)\} = 0 \qquad \text{for } x = x_{max}, \tag{8}$$

where $j_k(= -D_k \frac{\partial n_k}{\partial x} + v_k n_k)$ is the flux (current density) and D_k is the diffusion coefficient of charged species k by the Einstein relationship. The drift velocities of the charged species k are given by $v_k = \mu_k E = \frac{q_e E}{\gamma_k}$, where μ_k is the mobility, q_e is the unit charge, E is the electric field, and γ_k is the friction coefficient related to the product of mass and momentum-transfer collision frequency. Meanwhile, when a negative ac voltage $[V(0, t) < 0]$ is applied in the $+x$ direction, the fuel and oxygen sides switch to the opposite boundary conditions, as expressed in Eqs. (9) and (10) for $x = x_{min}$ and $x = x_{max}$, respectively.

$$\{n_+(0, t), j_-(0, t), j_e(0, t)\} = 0 \qquad \text{for } x = x_{min}, \tag{9}$$

$$\{j_+(L, t), n_-(L, t), n_e(L, t)\} = 0 \qquad \text{for } x = x_{max}, \tag{10}$$

Although the details of the governing equations have been reported previously [25], the 1D ionic transport model applied in this transient analysis is briefly rewritten in the following. A global reaction mechanism comprises one chemi-ionization and two recombination reactions:

$$Fuel + O_2 \overset{k_{FO}}{\rightarrow} 2A^+ + B^- + e^- \quad \text{for chemi} - \text{ionization}, \tag{11}$$

$$A^+ + B^- \overset{k_1}{\rightarrow} AB \quad \text{for recombination 1}, \tag{12}$$

$$A^+ + e^- \overset{k_2}{\rightarrow} A \quad \text{for recombination 2}, \tag{13}$$
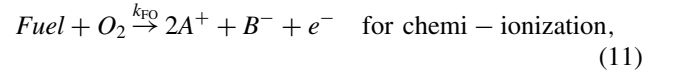
where $Fuel$ and O_2 are the supplied fuel and oxygen, respectively; A^+ and B^- are the intermediate ions; e^- is the intermediate electron appearing in the chemi-ionization; k_{FO}, k_1, and k_2 are the reaction rates in these irreversible reactions; AB and A are the combustion products by the recombinations. The time evolution of the number densities $n_i(x, t)$ are expressed as

$$\frac{\partial n_F}{\partial t} - D_F \frac{\partial^2 n_F}{\partial x^2} + v_F \frac{\partial n_F}{\partial x} = -k_{FO} n_F n_O, \tag{14}$$

$$\frac{\partial n_O}{\partial t} - D_O \frac{\partial^2 n_O}{\partial x^2} + v_O \frac{\partial n_O}{\partial x} = -k_{FO} n_O n_F, \tag{15}$$

$$\frac{\partial n_+}{\partial t} - D_+ \frac{\partial^2 n_+}{\partial x^2} + v_+ \frac{\partial n_+}{\partial x} = 2k_{FO} n_F n_O - k_1 n_+ n_- - k_2 n_+ n_e, \tag{16}$$

$$\frac{\partial n_-}{\partial t} - D_- \frac{\partial^2 n_-}{\partial x^2} + v_- \frac{\partial n_-}{\partial x} = k_{FO} n_F n_O - k_1 n_+ n_-, \quad (17)$$

$$\frac{\partial n_e}{\partial t} - D_e \frac{\partial^2 n_e}{\partial x^2} + v_e \frac{\partial n_e}{\partial x} = k_{FO} n_F n_O - k_2 n_+ n_e, \quad (18)$$

where D_i is the diffusion coefficient and v_i is the drift velocity. The chemi-ionization reaction rate k_{FO} is assumed to be proportional to the product of the number densities of fuel and oxygen as $k_{FO} = K_F (n_F n_O)$, where K_F is a parameter for determining the strength of the chemi-ionization reaction rate. The local electric field as a function of x can be deduced from the electric potential as $E(x) = -\frac{\partial V(x)}{\partial x}$, and $V(x)$ is determined by Poisson's equation of $\frac{\partial^2 V(x)}{\partial x^2} = -\frac{q_e}{\varepsilon}(n_+ - n_- - n_e)$, where ε is the permittivity of vacuum.

The average flow (drift) velocities of fuel and oxygen are modeled simply as

$$v_F = v_{F,S} + v_M, \quad (19)$$

$$v_O = v_{O,S} + v_M. \quad (20)$$

As the first terms on the right-hand side of Eqs. (19) and (20), $v_{F,S}$ and $v_{O,S}$ are the base velocities of fuel and oxygen, which are modeled by considering the axial velocity variations owing to the positive divergence of the opposed-nozzle flow field along the centerline, as a linear function of x, respectively:

$$v_{F,S} = \begin{cases} v_{F,0}\left(1 - \frac{x - x_{\min}}{0.5 x_{\max}}\right) & \text{for } 0 \leqslant x \leqslant \frac{L}{2} \\ 0 & \text{for } \frac{L}{2} \leqslant x \leqslant L \end{cases}, \quad (21)$$

$$v_{O,S} = \begin{cases} 0 & \text{for } 0 \leqslant x \leqslant \frac{L}{2} \\ -v_{O,0}\left(1 - \frac{x_{\min} - x}{0.5 x_{\max}}\right) & \text{for } \frac{L}{2} \leqslant x \leqslant L \end{cases}, \quad (22)$$

where $v_{F,0}$ and $v_{O,0}$ are the initial velocities of fuel and oxygen at the nozzle exits, respectively. As the second term, v_M is the correction velocity in the fuel and oxygen as a function of charged species flux:

$$v_M = K_m(n_+ v_+) \quad \text{for OIW}, \quad (23)$$

$$v_M = K_m(n_+ v_+ + n_- v_- + n_e v_e) \quad \text{for TIW}, \quad (24)$$

where K_m is a parameter in determining the strength of the flow retardation.

This 1D ionic transport model derived above demonstrated that it could successfully reproduce the interesting features of the counterflow diffusion flame responses in dc electric fields by comparing OIW and TIW effects [25]. Therefore, the physical constants used in the present model and the reference values for scaling dimensionless quantities to obtain numerical stability were valid and identical to those of previous studies [25,38–42], as listed in Tables I and II. Using the Engineering Equation Solver with a high-order predictor-corrector algorithm [43], the spatially discretized dimensionless governing equations for a uniform element with 80 nodes were numerically solved in the transient mode of ac electric fields. The present calculations satisfied the numerical stability with

TABLE I. Constants for ionic transport model.

Constant		Note
D_- [cm^2/s]	0.043	Ref. [40]
D_+ [cm^2/s]	0.028	Ref. [40]
D_e [cm^2/s]	0.043×10^4	Simply assumed as $D_- \times 10^4$
D_F [cm^2/s]	0.217	Ref. [41]
D_O [cm^2/s]	0.176	Ref. [42]
k_1 [cm^3/no. s]	2.4×10^{-7}	Ref. [39]
k_2 [cm^3/no. s]	2.4×10^{-7}	Ref. [39]
q_e [C]	1.6×10^{-19}	Ref. [39]
$v_{F,0}$ [cm/s]	30	Present experiment
$v_{O,0}$ [cm/s]	30	Present experiment
μ_- [cm^2/V s]	2.9	Ref. [39]
μ_+ [cm^2/V s]	2.9	Ref. [39]
μ_e [cm^2/V s]	0.4×10^4	Ref. [39]
L [cm]	1.6	Present experiment
ε [C/V cm]	8.854×10^{-12}	Ref. [39]

CFL = 0.001–0.03 based on the Courant criteria. Here, the $\tilde{K}_F$ in the chemi-ionization reaction rate increased until the dimensionless number density of fuel and oxygen decreased to below 10^{-6} around the nozzles on each opposing side [25]. The $\tilde{K}_m$ increased until the flame positions reached near the maximum limits at the applied ac voltage of $\tilde{V}_{ac} = 10$, and $\tilde{K}_m = 500$ in the correction velocity was selected with respect to the OIW and TIW models.

As described in the equations, the fuel and oxygen are injected at the opposite nozzle exits and transported by the convection terms of the linear base velocities together with the diffusion terms. When there is no electric field, the generation of an ionic layer that substitutes for the counterflow diffusion flame occurs in the middle position. When the electric fields are applied, the positive and negative ions as well as electrons produced by the chemi-ionization process have the bidirectional drift velocities as the product of their mobility and the strength of electric fields. Regarding the interplay through a momentum transfer, the sum of all the charged species fluxes was coupled with the bulk flow velocities of the fuel and oxygen to reflect the collisional effect on the neutral particles. Hence, the proposed model leads to a change in the distributions of the central ionic layer according to the ionic wind effect attributed to the applied electric fields, and allows a qualitative analysis and cost-effective computation specific to the nonlinear flame responses.

TABLE II. Reference values for nondimensionalization.

	Reference value for dimensionless quantity
n_a [no./cm^3]	6.02×10^{23} [ions/liter] $\approx 3 \times 10^{19}$ [ions/cm^3]
n_0 [no./cm^3]	$n_a \times (1 \times 10^{-2} \text{ [cm/}x_0])^3 \approx 10^{13}$ [ions/x_0^3]
$q_{e,0}$ [C]	1×10^{-19}
t_0 [s]	1×10^{-1}
V_0 [V]	1×10^2
x_0 [cm]	1×10^{-2}
ε_0 [C/V cm]	$\frac{q_{e,0}}{V_0 x_0}$

(a)

(b)
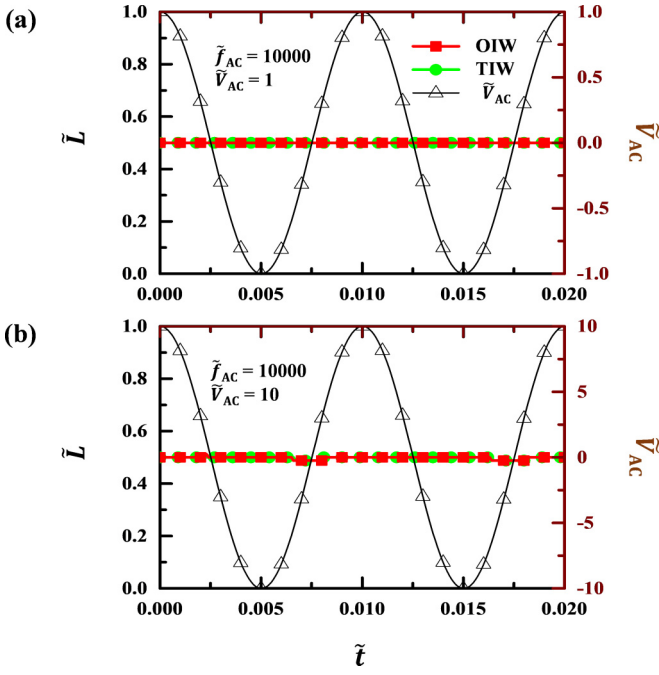
FIG. 5. Stable flame positions for (a) $(\tilde{f}_{\rm ac}, \tilde{V}_{\rm ac}) = (10\,000, 1)$ and (b) $(10\,000, 10)$ with respect to the OIW and TIW models.

It is noted that the radial flame shapes as shown in Fig. 2(b) are curved under the various ac electric fields. The radial profiles were more severely distorted outside the nozzle diameter ($r/R > 1$). This is indicative that the self-similarity assumptions for the thermo-flow field can be less preserved for the electrified flames in an insufficiently slender burner with the

aspect ratio of $2R/L = 1$ [44]. Such a multidimensionality effect on the flow-chemistry interaction in no electrified flames can be revealed clearly through an extreme comparison of 1D counterflow and 2D axisymmetric coflow nonpremixed flames (i.e., such aspect ratios of $2R/L \approx \infty$ and ≈ 0) [45]. Nevertheless, our 1D approach was simply limited as a function of x with no consideration of the radial variations and we mainly focused on the qualitative characteristics of the flame positions along the centerline in the present unsteady and previous steady analyses [25].

V. NUMERICAL RESULTS AND DISCUSSION

A. Dynamic flame positions responding to sine function electric fields

As a relatively high ac frequency, when $\tilde{f}_{\rm ac}$ was fixed at 10 000, the responses of the flame positions were represented with regard to the OIW and TIW models, as shown in Figs. 5(a) $\tilde{V}_{\rm ac} = 1$ and (b) 10, respectively. The flame positions were not changed from $\tilde{L} = 0.5$ for $\tilde{V}_{\rm ac} = 1$ and maintained at the middle position with a slight deviation of $\pm\,0.0125$ for $\tilde{V}_{\rm ac} = 10$. According to the conditions of $\tilde{f}_{\rm ac}$ and $\tilde{V}_{\rm ac}$ in Fig. 5(b), the typical profiles of the dimensionless number densities of $\tilde{n}_{\rm F}$ and $\tilde{n}_{\rm O}$ and dimensionless reaction rate of $\tilde{k}_{\rm FO}$ were plotted as a function of dimensionless nozzle distance of $\tilde{L}$, as shown in Fig. 6(a). Despite the phase changes in the applied ac voltages of $\pm\pi/2$, their profiles remained almost uniform regardless of the OIW and TIW models. Furthermore, in Fig. 6(b), the profiles of the dimensionless number densities of $\tilde{n}_{+}$, $\tilde{n}_{-}$, and $\tilde{n}_{\rm e}$ exhibited similar distributions from their

(a)   **(c)**

(b)   **(d)**
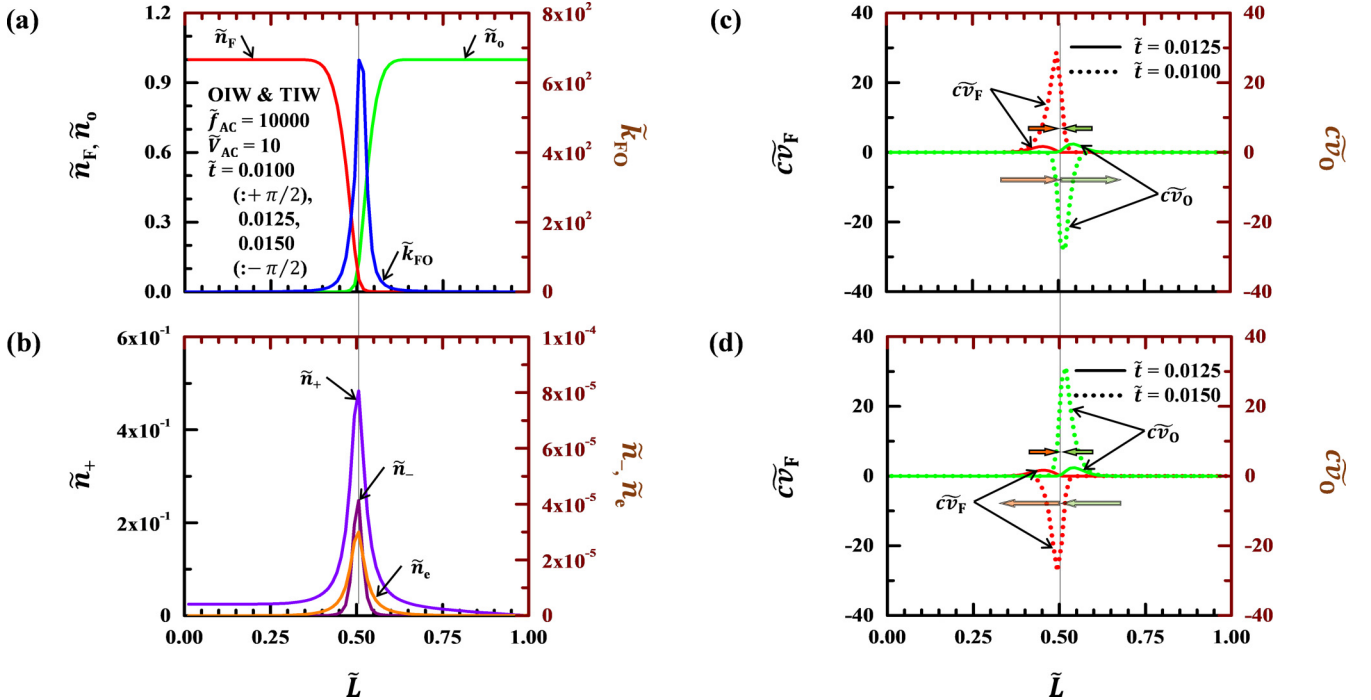
FIG. 6. Profiles of dimensionless quantities as a function of $\tilde{L}$ for $(\tilde{f}_{\rm ac}, \tilde{V}_{\rm ac}) = (10\,000, 10)$: (a) $\tilde{n}_{\rm F}$, $\tilde{n}_{\rm O}$, and $\tilde{k}_{\rm FO}$, (b) $\tilde{n}_{+}$, $\tilde{n}_{-}$, and $\tilde{n}_{\rm e}$, (c) $\widetilde{cv}_{\rm F}$ and $\widetilde{cv}_{\rm O}$ marked as solid line for $\tilde{t} = 0.0125$ and dotted line for $\tilde{t} = 0.0100$ (:$+\pi/2$), (d) $\widetilde{cv}_{\rm F}$ and $\widetilde{cv}_{\rm O}$ marked as solid line: $\tilde{t} = 0.0125$ and dotted line for $\tilde{t} = 0.0150$ (:$-\pi/2$), with respect to the OIW and TIW models.
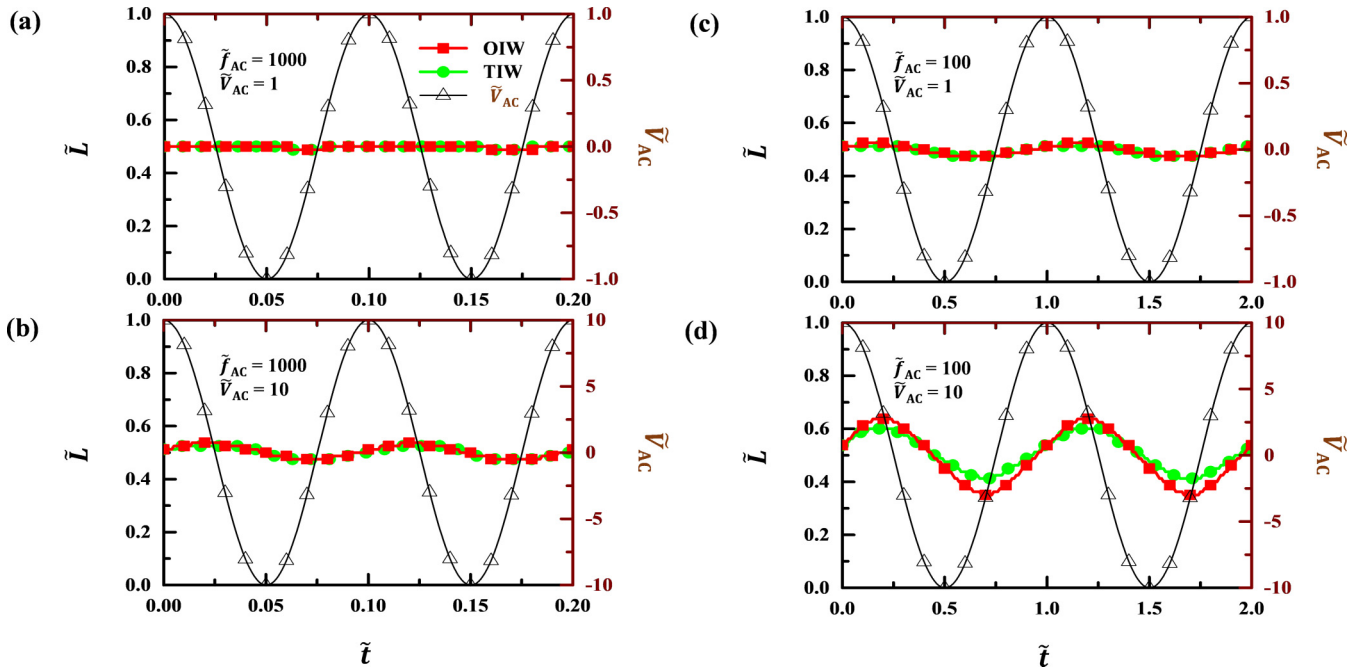
FIG. 7. Sinusoidally oscillating flame positions for (a) $(\tilde{f}_{ac}, \tilde{V}_{ac}) = (1000, 1)$, (b) (1000, 10), (c) (100, 1), and (d) (100, 10) with respect to the OIW and TIW models.

peak positions, which corresponded to that of the $\tilde{k}_{FO}$ profile, toward both the nozzle exits.

For $\tilde{t} = 0.0125$ shown in Figs. 6(c)–6(d), the profiles of the dimensionless convective terms of $\widetilde{cv}_F$ and $\widetilde{cv}_O$ of the fuel and oxygen flows acted in the opposite direction (indicated by arrows in the figure). This was similar with the case of no electric field and enabled the ionized layer to stabilize at approximately the midpoint, where the counterflowing fuel and oxygen were stagnant (solid line with gray). However, both the convective terms acted in the same direction toward the oxidizer side of $\tilde{L} = 1$ at $\tilde{t} = 0.0100$ (:$+\pi/2$) [Fig. 6(c)] and the fuel side of $\tilde{L} = 0$ at $\tilde{t} = 0.0150$ (:$-\pi/2$) [Fig. 6(d)], respectively. Additionally, their magnitudes became significantly higher than those of $\tilde{t} = 0.0125$, but no distinctive movement occurred in the flame position, as shown in Fig. 5(b).

For the intermediate ac frequency, Fig. 7 shows the flame positions responding to (a) $(\tilde{f}_{ac}, \tilde{V}_{ac}) = (1000, 1)$, (b) (1000, 10), (c) (100, 10), and (d) (100, 10) with respect to the OIW and TIW models. The response of the flame position was negligibly small when $(\tilde{f}_{ac}, \tilde{V}_{ac}) = (1000, 1)$ was applied. When the applied voltage increased with $\tilde{V}_{ac} = 10$ [Fig. 7(b)] or the applied frequency decreased with $\tilde{f}_{ac} = 100$ [Fig. 7(c)], compared with the condition in Fig. 7(a), the time evolution of the flame position exhibited a sinusoidal motion. In the case of Fig. 7(d) when both conditions were applied, the amplitude of the sinusoidal oscillation increased distinctively and the amplitude of the OIW model was larger than that of the TIW model.

For the representative conditions in Fig. 7(d), the profiles of the dimensionless values are presented with respect to the (a) OIW and (b) TIW models in Fig. 8. For the OIW model, the $\tilde{k}_{FO}$ profile shifted in the reverse direction toward the oxidizer side of $\tilde{L} = 1$ at $\tilde{t} = 1.0$ (:$+\pi/2$) and the fuel side of $\tilde{L} = 0$ at $\tilde{t} = 1.5$ (:$-\pi/2$) in Fig. 8(a-i). The peak position

of the $\tilde{k}_{FO}$ profile was located at approximately the midpoint, where the counterflowing fuel and oxygen were stagnant (solid and dotted gray lines). According to the movement of the ionic layer, all positions of the peak number densities of the charged species migrated repeatedly toward the oxidizer and fuel sides, as shown in Fig. 8(a-ii). In particular, the profiles of $\tilde{n}_-$ and $\tilde{n}_e$ moved promptly including within a single peak of the ionic layer, but the $\tilde{n}_+$ profiles showed relatively slow responses while exhibiting two broad afterimages in both directions from their peak positions, owing to the richer concentration and smaller diffusion coefficient.

In these cases, the profiles of $\widetilde{cv}_F$ and $\widetilde{cv}_O$ in Fig. 8(a-iii) show convection in the same direction acting toward each of the flow stagnation. In Fig. 8(b) illustrating the TIW model, although the overall profiles of the dimensionless number densities are similar to those of the OIW model in Fig. 8(a), the peak values are relatively large, and the distance between the stagnation points is relatively small. Figure 8(b-iii) shows that the different profiles in the TIW model can result from additional convections of fuel and oxygen acting against the opposite direction to the movement of the flame positions.

For the relatively low ac frequency, Fig. 9 shows the flame positions responding to (a) $(\tilde{f}_{ac}, \tilde{V}_{ac}) = (10, 1)$, (10, 1), (b) (10, 10), (c) (1, 1), and (d) (1, 10) with respect to the OIW and TIW models. For $\tilde{V}_{ac} = 1$, the magnitudes of the sinusoidally oscillating flame position increased slightly with the decrease in the applied ac frequency from $\tilde{f}_{ac} = 100$ in Fig. 7(c) to $\tilde{f}_{ac} = 1$ in Fig. 9(a). No significant difference was observed in the flame responses between (a) $(\tilde{f}_{ac}, \tilde{V}_{ac}) = (10, 1)$ (10, 1) and (c) (1. 1) in Fig. 9, as well as in the OIW and TIW models. However, for $\tilde{V}_{ac} = 10$, the response of the flame positions for $\tilde{f}_{ac} = 10$ in Fig. 9(b) showed a nonmonotonic behavior with time. When the slope of the applied ac voltage was reversed,
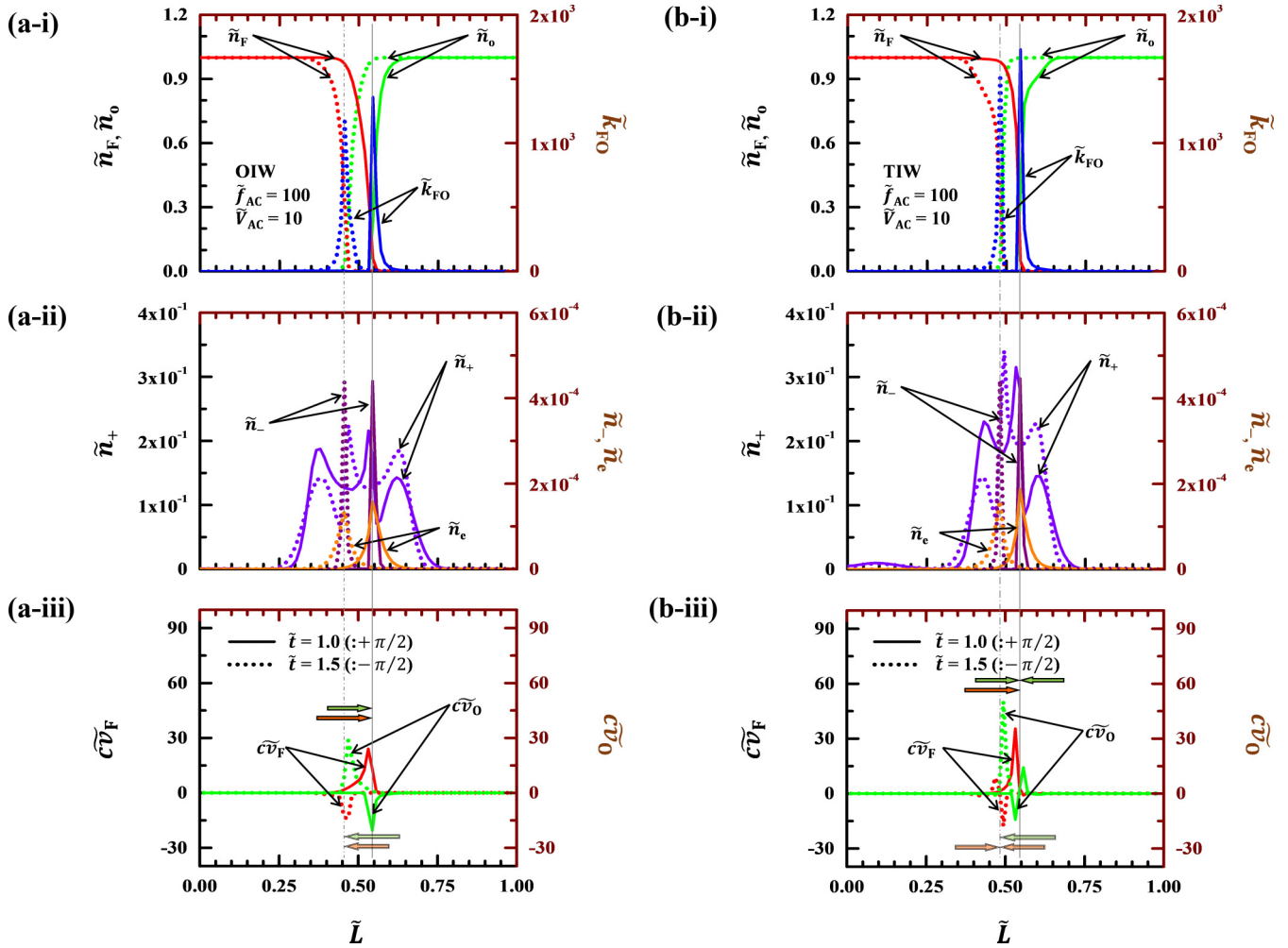
FIG. 8. Profiles of dimensionless quantities as a function of $\tilde{L}$ for $(\tilde{f}_{ac}, \tilde{V}_{ac} =) = (100, 10)$: (i) $\tilde{n}_F$, $\tilde{n}_O$, and $\tilde{k}_{FO}$, (ii) $\tilde{n}_+$, $\tilde{n}_-$, and $\tilde{n}_e$, (iii) $\widetilde{cv}_F$ and $\widetilde{cv}_O$, marked as solid line: $\tilde{t} = 1.0$ $(:+\pi/2)$ and dotted line for $\tilde{t} = 1.5$ $(:-\pi/2)$, with respect to the (a) OIW and (b) TIW models.

the flame positions jumped up or down momentarily, and the distance of momentary shift for the TIW model was larger than that of the OIW model. This numerically reproduced the behavior of the momentary shifting flame position, which resembled the experimental jumping down behavior during the period when the flame positions were shifted toward the upper oxidizer side for $(f_{ac}, V_{ac}) = (2$ Hz, 0.8 kV) (2 Hz, 0.8 kV) as shown in Fig. 3(b).

When the applied ac frequency was further reduced to $\tilde{f}_{ac} = 1$, as shown in Fig. 9(d), a nonmonotonic oscillation of the flame positions appeared with the forced oscillation of the sine wave synchronized by the applied ac frequency, in which the frequency of the remarkable harmonic oscillation exhibited higher values than that of the applied ac frequency. Additionally, the amplitude and frequency of the harmonic flame oscillation for the TIW model was relatively large and lower, respectively, compared with those of the OIW model. These harmonic oscillations were consistent with the OIW and TIW models resembled partially by the experimental results of the momentary falling-down motion with two sharp points in the lower fuel side for $f_{ac}, V_{ac} = (0.2$ Hz, 2.0 kV), as shown in Fig. 3(c). Consequently, the nonmonotonic change

in the flame positions shown in Figs. 9(b) $(\tilde{f}_{ac}, \tilde{V}_{ac}) = (10, 10)$ and 9(d) $(1, 10)$ implies that the important features in the experimental results of the dynamic flame positions for the relatively low ac frequency can be effectively reproduced by the proposed 1D model adopting not only the OIW model, but also the TIW model.

To compare with the experimental results, Fig. 10 shows the representative flame responses during one cycle of the dimensionless period $\tilde{T} = 1$ for (a) the intermediate and (b) relatively low ac frequency regions. For $(\tilde{f}_{ac}, \tilde{V}_{ac}) = (100, 10)$ in Fig. 10(a), the flame positions of the OIW and TIW results were good agreement with those of the experimental results, while both the OIW and TIW models did not reflect that the experimental results were slightly shifted and magnified in the upward direction. For $(\tilde{f}_{ac}, \tilde{V}_{ac}) = (1, 10)$ in Fig. 10(b), when the negative ac voltages were applied, the harmonic oscillation of the TIW model exhibiting the larger amplitude and lower frequency was more similar to the experimental results exhibiting the momentary falling-down motion. When the positive ac voltages were applied, the harmonic oscillation of the OIW model exhibiting the smaller amplitude and higher frequency was more similar to the experimental
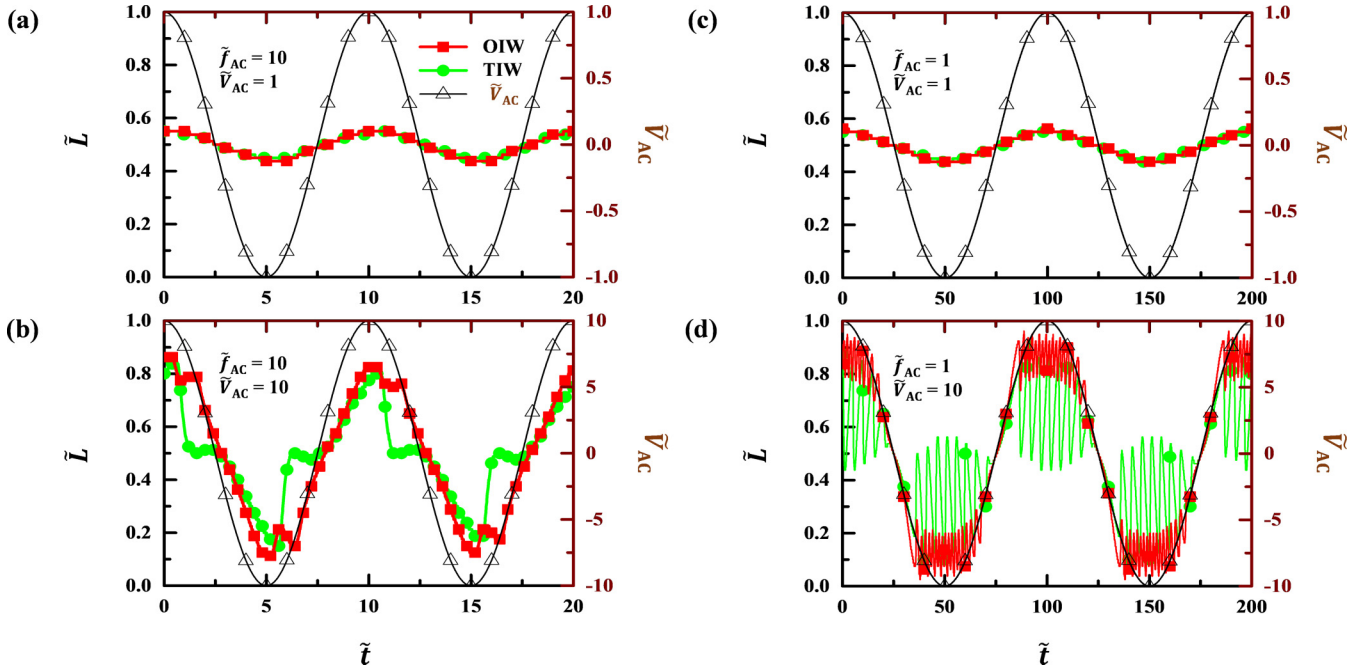
FIG. 9. Nonmonotonically or sinusoidally oscillating flame positions for (a) $(\tilde{f}_{ac}, \tilde{V}_{ac}) = (10, 1)$, (b) (10, 10), (c) (1, 1), and (d) (1, 10) with respect to the OIW and TIW models.

results exhibiting the fluctuation motion. However, neither the OIW nor TIW models reflected quantitatively that the experimental results showed the different responses in the upward and downward directions. As mentioned in the experimental part in Sec. III and Ref. [25], the difference between the upward and downward dynamic behaviors in the experimental results may be resulted from the gravitational interference of the buoyancy effects acting upwards on a reaction zone

with relatively low density. That is, when the direction of the applied electric field acts in the same or opposite to that of the buoyancy, the movement of the flame positions can be promoted or inhibited. Therefore, further studies are needed to implement additional models for the buoyancy effects in the 1D ionic transport equations.

The previous dc study [25] reported that the TIW model rather than the OIW model in our 1D ionic transport model
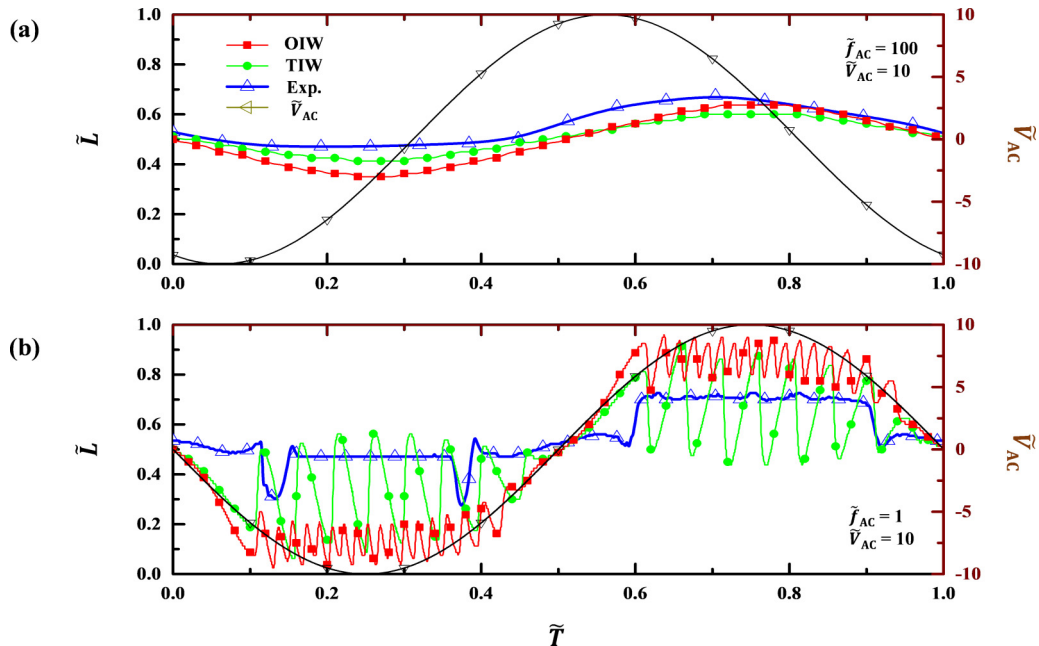
FIG. 10. Comparison of experimental data with nonmonotonically or sinusoidally oscillating flame positions for (a) $(\tilde{f}_{ac}, \tilde{V}_{ac}) = (100, 10)$ and (b) (1, 10) with respect to the OIW and TIW models.
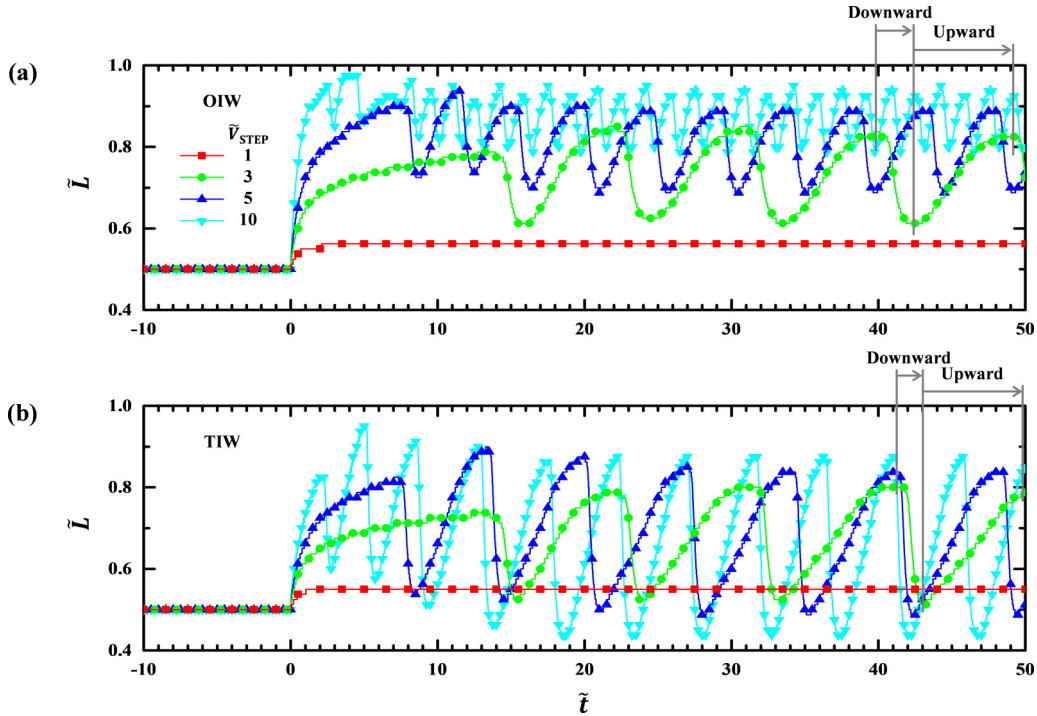
FIG. 11. Dynamic flame positions responding to $\tilde{V}_{STEP} = 1, 3, 5, 10$ with respect to the (a) OIW and (b) TIW models.

showed the ability to produce the double peaks in the ionic layer accompanied by the three stagnation points. In the relatively high ac frequency region of the present study, no significant separation between the fuel and oxygen profiles for $(\tilde{\tilde{f}}_{ac}, \tilde{V}_{ac}) = (10\,000, 10))$ was observed for the numerical conditions in the present ac simulations, as shown in Fig. 6. The results are reasonable in terms of requiring the collision response time to induce the ionic wind effect. Besides, although not shown in a figure, the numerical results for $(\tilde{f}_{ac}, \tilde{V}_{ac}) = (10\,000, 100)$ exhibited no distinctive difference to the results in Fig. 6. However, this is inconsistent with the visualization results that the flow separation phenomenon observed in the dc experiment [20] occurs also in the relatively high ac frequency [33]. It requires a detailed study in the future.

B. Dynamic flame positions responding to step function electric fields

To identify the underlying mechanism for the nonmonotonically oscillating behaviors of the flame positions specific to the relatively low ac frequency, the sine-function ac voltage in Eq. (5) was replaced with a step function, which exhibited $\tilde{V}_{STEP} = 0$ for $\tilde{t} \leqslant 0$ and constant values of $\tilde{V}_{STEP}$ for $\tilde{t} > 0$. Furthermore, the dynamic responses at the flame positions were recorded with time according to the (a) OIW and (b) TIW models in Fig. 11. For the OIW model in Fig. 11(a), the flame position as a function of time for $\tilde{V}_{STEP} = 1$ exhibited a constant value after settling $\tilde{t} \approx 2$. However, for $\tilde{V}_{STEP} = 3$, 5, and 10, the flame positions started to oscillate significantly after experiencing their rising times despite the uniform electric potential differences between the cathode and anode electrodes, which is similar to case of dc electric fields. Because the flame oscillation was activated by an impulse,

which is the derivative value of $\tilde{V}_{STEP}$ at $\tilde{t} = 0$, the dynamic flame motions in the stepwise electric fields could be regarded as free oscillations, including its natural frequency. Additionally, free oscillations appeared in the TIW model, as shown in Fig. 11(b); however, the major features of their natural frequencies and amplitudes were distinctively distinguishable in accordance with the applied $\tilde{V}_{STEP}$ voltages.

Figure 12(a) shows the inverse of the dimensionless time for the free oscillation period in the stable state as a function of the applied $\tilde{V}_{STEP}$ voltage with respect to the OIW and TIW models. When $\tilde{V}_{STEP} = 3$, the dimensionless natural frequency was similar to $1/\tilde{T} \approx 0.1$. As $\tilde{V}_{STEP}$ increased, the free oscillation of the OIW model became faster than that of the TIW model. The deviation in the natural frequency $f_{natural}$ according to the ionic wind models exhibited a wide range of $f_{natural} = 1$–6 Hz. This numerical value of the natural frequency agreed well with the experimental value of 5 Hz for the periodical oscillation under a constant dc voltage of $V_{dc} = -1.5$ kV observed in the previous study [25], as mentioned in Sec. III. Therefore, free oscillations under the applied $\tilde{V}_{STEP}$ voltages could be considered as a main cause of the findings. This resulted in not only nonmonotonic behaviors for the relatively low ac frequencies [such as the harmonic oscillations represented in Figs. 9(b) and 9(d)], but also the oscillating and fluctuating responses of the flame positions exhibiting instability in the certain ranges of the applied dc voltages [25]. This implies the following: (1) the nonmonotonic response of the flame positions can be effectively reproduced by applying any model (either the OIW model or the TIW model) and (2) the behavior between the dynamical flame positions responding to both the slowly varying ac and constant dc electric fields, as shown in Fig. 2(a-iii), can result from the natural frequency of the ionic system.
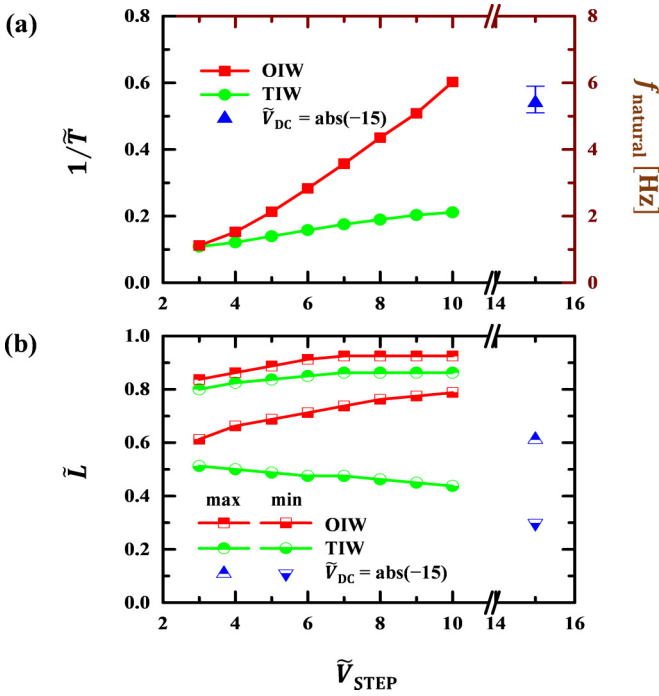
FIG. 12. (a) inverse of dimensionless period and natural frequency and (b) maximum and minimum flame positions as a function of $\tilde{V}_{STEP}$ with respect to the OIW and TIW models, comparing with the free oscillation under $V_{dc} = -1.5$ kV [25].

As shown in Fig. 12(b), as the applied $\tilde{V}_{STEP}$ voltage increased, the maximum positions for the freely oscillating flame positions saturated at $\tilde{L} \approx 1$, and were slightly lower in the case of the TIW model compared with the OIW model. For the OIW model, the minimum positions increased and the amplitude of the free oscillation decreased with $\tilde{V}_{STEP}$. In contrast to the OIW model, the minimum positions for the TIW model decreased significantly, accompanied by an increase in the amplitude of the free oscillations with $\tilde{V}_{STEP}$. Consequently, it could be deduced that the different responses of the minimum flame positions with the $\tilde{V}_{STEP}$ function might generate different responses in the OIW and TIW models, as shown in Figs. 9(b) and 9(d), for the relatively low ac frequency.

To elucidate the physical origin governing the free oscillations in the ionic system, the downward and upward movements of the flame positions (marked as arrows in Fig. 11) were further investigated for the representative case where the positive constant voltage of $\tilde{V}_{STEP} = 3$ was applied to the lower fuel side of $\tilde{L} = 0$ (anode electrode). For the downward movements of the flame positions, the time evolution profiles of the dimensionless number densities and convection terms were compared with respect to the (a) OIW and (b) TIW models in Fig. 13. For the OIW model in Fig. 13(a-i), the peak positions of $\tilde{k}_{FO}$ profiles, which was formed at the stagnation point (solid line with gray) between the fuel and oxidizer profiles, shifted down gradually from the maximum position in the upper oxidizer side (ground electrode) toward the lower fuel side. Subsequently, the magnitude of their peak values represented a reducing tendency. At this moment, in Fig. 13(a-ii), the $\tilde{n}_-$ and $\tilde{n}_e$ profiles became higher and wider toward the anode electrode, and their peak positions

were coupled with the stagnation points. However, the $\tilde{n}_+$ profiles exhibited a delaying tendency to maintain the previous $\tilde{n}_+$ profile located at the maximum flame position and newly generated a secondary peak, which shifted remarkably toward the lower fuel side and coupled with the stagnation point. These trends in the profiles of the OIW model in Figs. 13(a-i) and 13(a-ii) were similar to those of the TIW model in Figs. 13(b-i) and 13(b-ii), respectively.

For the OIW model in Fig. 13(a-iii), the convection profiles of $\widetilde{cv}_F$ and $\widetilde{cv}_O$ acted against the opposite direction of the flow stagnation (solid line with gray) while shifting toward the lower fuel side. However, for the TIW model in Fig. 13(b-iii), the time evolution profiles of $\widetilde{cv}_F$ and $\widetilde{cv}_O$ represented a transition from the opposite direction to the same direction toward the lower fuel side, in which the flow stagnations and $\tilde{k}_{FO}$ peaks maintained with time as the single points equal to the OIW model. The difference in convective behavior between the ionic wind models resulted in faster and longer displacements during $\tilde{t} = 42.2$–42.5 in the TIW model, as compared with those of $\tilde{t} = 41.3$–41.9 in the OIW model. Therefore, this accelerating motion could result in a significant moving down of the minimum positions and increasing amplitude for the free oscillations in the case of the TIW model rather than the OIW model, as shown in Fig. 12(b).

For the upward movements of the flame positions, the time evolution profiles of the dimensionless number densities and convection terms are shown with respect to the OIW (a) and TIW (b) models in Fig. 14. In particular, the upward movements exhibited a relatively slow motion compared with that of the downward movements, as shown in Fig. 11. For the OIW model in Fig. 14(a-i), the positions and magnitudes of the $\tilde{k}_{FO}$ peaks gradually reshaped toward the upper oxidizer side (ground electrode). In recovering the flame positions upwardly, the $\tilde{n}_+$, $\tilde{n}_-$, and $\tilde{n}_e$ profiles tended to maintain single peaks coupled with stagnation points under a slower motion, as shown in Fig. 14(a-ii). The generation of $\tilde{n}_-$ and $\tilde{n}_e$ peaks was relatively low compared with those of the downward movements. As shown in Fig. 14(a-iii), the $\widetilde{cv}_F$ and $\widetilde{cv}_O$ profiles acted primarily in the opposite directions against the flow stagnations, but the additional convection term of $\widetilde{cv}_O$ was continuously exerted in the same direction as that of the upward movement. These trends in the profiles of the OIW model in Fig. 14(a) are similar to those of the TIW model in Fig. 14(b).

Consequently, the detailed mechanism for the free oscillations of the 1D ionic model specific to the constant $\tilde{V}_{STEP}$ voltage applied to the lower fuel side can be explained based on the electrostatic forces for the reflecting and absorbing boundary conditions in Eq. (8). This implies that a repulsive force by the identical polarities between the negatively charged species ($\tilde{n}_-$ and $\tilde{n}_e$) and the ground electrode can be activated locally when the ionized layer reached near the upper oxidizer side. The positive ions tended to remain near the upper oxidizer side by the attractive force between the positively charged ion ($\tilde{n}_+$) and the ground electrode; however, the repulsive force of the negatively charged species resulted in the downward movement of $\tilde{k}_{FO}$ peaks coupled with the flow stagnation between the counterflowing fuel and oxygen. This was accompanied by the secondary peaks of positive ions generated by the chemi-ionization
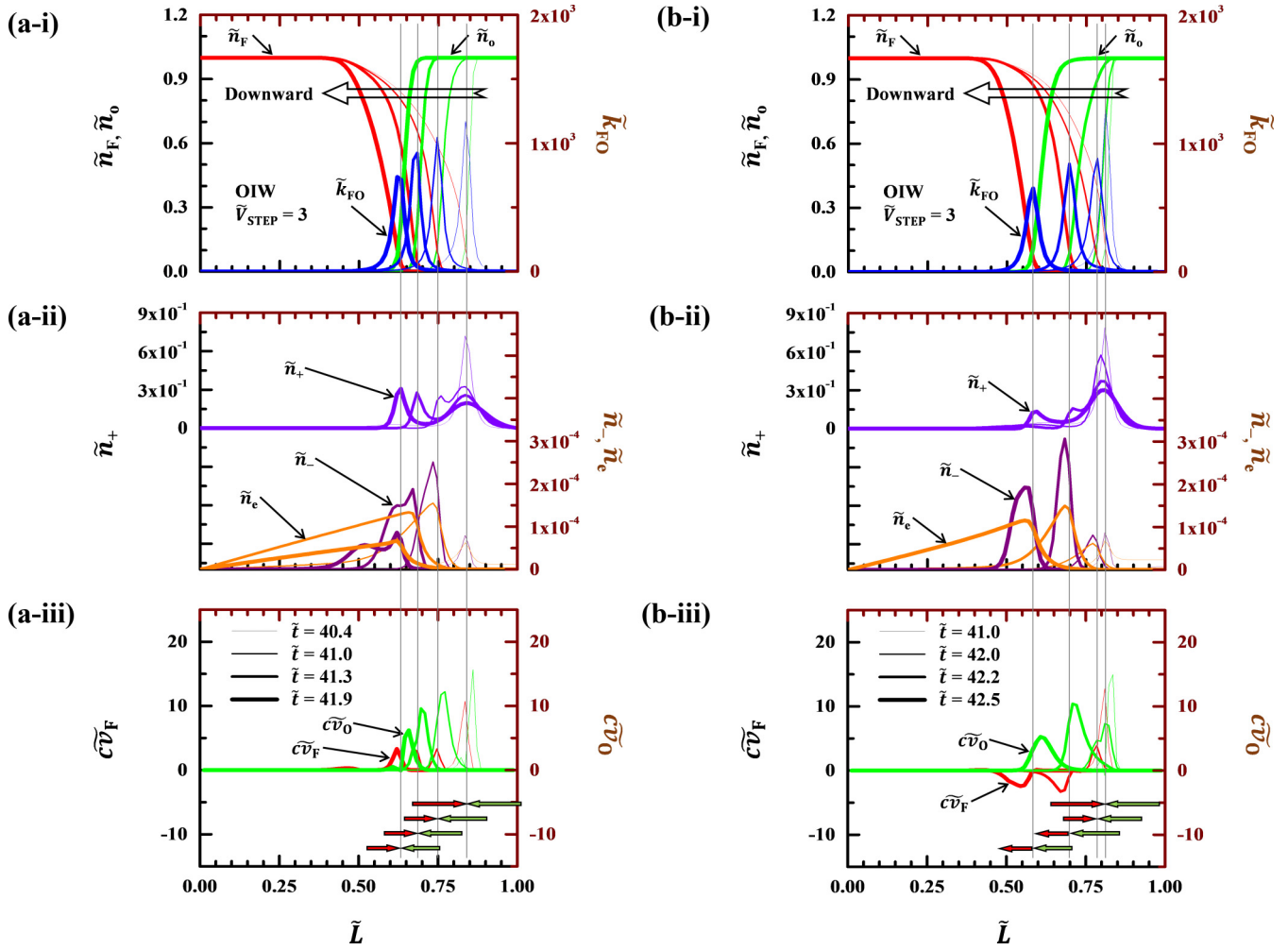
FIG. 13. Sequential profiles of dimensionless quantities as a function of $\tilde{L}$ for downward movement responding to $\tilde{V}_{STEP} = 3$: (i) $\tilde{n}_F$, $\tilde{n}_O$, and $\tilde{k}_{FO}$, (ii) $\tilde{n}_+$, $\tilde{n}_-$, and $\tilde{n}_e$, (iii) $\widetilde{cv}_F$ and $\widetilde{cv}_O$, with respect to the (a) OIW and (b) TIW models.

in Eq. (11). After the charged species profiles were redistributed by recombinations 1 and 2 in Eqs. (12) and (13), the flame positions started to move toward the upper oxidizer side because the ionic wind effect induced by the electric (Lorentz) force became dominant again under the uniform difference in the electric potential. Therefore, the free oscillation could have originated from the repetitive balance between the repulsive and ionic wind-induced forces when sufficient response time was provided in the ionic system for both the OIW and TIW models.

VI. CONCLUDING REMARKS

Using the 1D ionic transport model, which was suggested by our previous study on dc electric fields [25], the dynamic response of flame positions was numerically investigated in ac and step electric fields to understand the experimental observations of nonmonotonic flame responses specific to relatively low ac frequencies and dc voltage ranges. The interesting features of the ionized layer in the applied ac voltages are summarized and compared with respect to the OIW and TIW models as follows.

For the relatively high ac frequency, the ionic profiles of $\tilde{k}_{FO}$, $\tilde{n}_+$, $\tilde{n}_-$, and $\tilde{n}_e$ and their peak positions were maintained near the middle position and were almost identical to those of the typical profile without any electric field. Their profiles remained almost uniform, even though the dimensionless convective terms of $\widetilde{cv}_F$ and $\widetilde{cv}_O$ in the OIW and TIW models were conversely affected by the phase changes in the applied ac voltages as $\pm\pi/2$. However, for the relatively low ac frequency, the flame positions exhibited a nonmonotonic oscillation composed of the forced oscillation synchronized by the applied ac voltages together with the free oscillation from the nonlinear ionic system. These harmonic oscillations in accordance with the OIW and TIW models resembled with the experimental results partially, exhibiting the momentary falling-down and jumping-up motions of the flame positions. In the intermediate ac frequency range, the flame positions represented a transition behavior between stable motion and sinusoidal oscillation.

Through a comparison of the free oscillations of the flame positions driven by the stepwise voltages in time, it was demonstrated that the harmonic oscillation in the relatively low ac frequency could have resulted from the free oscillation.
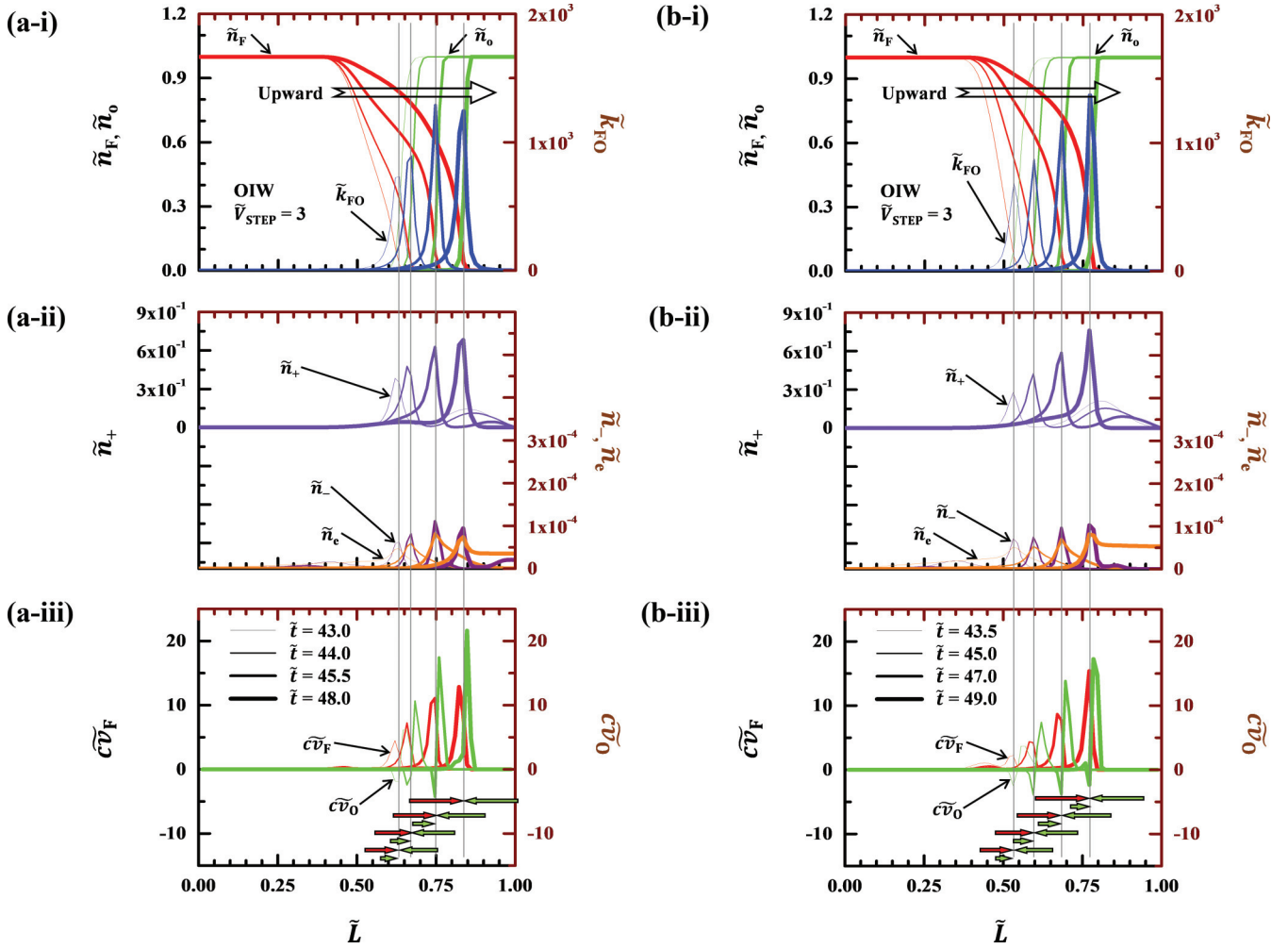
FIG. 14. Sequential profiles of dimensionless quantities as a function of $\tilde{L}$ for upward movement responding to $\tilde{V}_{STEP} = 3$: (i) $\tilde{n}_F$, $\tilde{n}_O$, and $\tilde{k}_{FO}$, (ii) $\tilde{n}_+$, $\tilde{n}_-$, and $\tilde{n}_e$, (iii) $\widetilde{cv}_F$ and $\widetilde{cv}_O$, with respect to the (a) OIW and (b) TIW models.

This originated from the interaction between the repulsive force and ionic wind-induced force in the ionic system, for both the OIW and TIW models. The numerical results agreed reasonably well with the distinctive features in the nonmonotonic responses of the ac experiments and suggested a possible solution that the present 1D ionic model could predict transient motions.

[1] S. A. Zonouzi, H. Aminfar, and M. Mohammadpourfard, A review on effects of magnetic fields and electric fields on boiling heat transfer and CHF, Appl. Therm. Eng. **151**, 11 (2019).

[2] G. Li, X. Jiang, J. Zhu, J. Yang, C. Liu, Y. Mu, and G. Xu, Combustion control using a lobed swirl injector and a plasma swirler, Appl. Therm. Eng. **152**, 92 (2019).

[3] H. Gotoda, Y. Okuno, K. Hayashi, and S. Tachibana, Characterization of degeneration process in combustion instability based on dynamical system theory, Phys. Rev. E **92**, 052906 (2015).

[4] A. Jocher and H. Pitsch, Combustion instability mitigation by magnetic fields, Phys. Rev. E **95**, 063113 (2017).

[5] D. G. Park, B. C. Choi, M. S. Cha, and S. H. Chung, Soot reduction under DC electric fields in counterflow non-premixed laminar ethylene flames, Combust. Sci. Technol. **186**, 644 (2014).

[6] M. Hase and S. N. Watanabe, Rhythmic motion of a droplet under a dc electric field, Phys. Rev. E **74**, 046301 (2006).

[7] J. Lawton and F. J. Weinberg, *Electrical Aspects of Combustion* (Clarendon Press, Oxford, 1969).

[8] F. J. Weinberg, *Advanced Combustion Methods* (Academic Press, London, 1986).

[9] A. B. Fialkov, Investigations on ions in flames, Prog. Energy. Combust. Sci. **23**, 399 (1993).

[10] J. M. Goodings, D. K. Bohme, and C. Ng, Detailed ion chemistry in methane-oxygen flames, I. Positive ions, Combust. Flame **36**, 27 (1979).

[11] J. Kuhl, G. Jovicic, L. Zigan, and A. Leipertz, Transient electric field response of laminar premixed flames, Proc. Combust. Inst. **34**, 3303 (2013).

[12] J. M. Goodings, D. K. Bohme, and C. Ng, Detailed ion chemistry in methane-oxygen flames, II. Negative ions, Combust. Flame **36**, 46 (1979).

[13] J. Prager, U. Riedel, and J. Warnatz, Modeling ion chemistry and charged species diffusion in lean methane-oxygen flames, Proc. Combust. Inst. **31**, 1129 (2007).

[14] M. Belhi, B. J. Lee, M. S. Cha, and H. G. Im, Three-dimensional simulation of ionic wind in a laminar premixed Bunsen flame subjected to a transverse DC electric field, Combust. Flame **202**, 90 (2019).

[15] M. Belhi, B. J. Lee, F. Bisetti, and H. G. Im, A computational study of the effects of DC electric fields on non-premixed counterflow mathane-air flames, J. Phys. D: Appl. Phys. 494005 (2017).

[16] M. Belhi, P. Domingo, and P. Vervisch, Modelling of the effect of DC and AC electric fields on the stability of a lifted diffusion methane/air flame, Combust. Theor. Model **17**, 749 (2013).

[17] M. Belhi, P. Domingo, and P. Vervisch, Direct numerical simulation of the effect of an electric field on flame stability, Combust. Flame **157**, 2286 (2010).

[18] J. Hu, B. Rivin, and E. Sher, The effect of an electric field on the shape of co-flowing and candle-type methane-air flames, Exp. Therm. Fluid Sci. **21**, 124 (2000).

[19] D. G. Park, S. H. Chung, and M. S. Cha, Visualization of ionic wind in laminar jet flames, Combust. Flame **184**, 246 (2017).

[20] D. G. Park, S. H. Chung, and M. S. Cha, Bidirectional ionic wind in nonpremixed counterflow flames with DC electric fields, Combust. Flame **168**, 138 (2016).

[21] G. T. Kim, D. G. Park, M. S. Cha, J. Park, and S. H. Chung, Flow instability in laminar jet flames driven by alternating current electric fields, Proc. Combust. Inst. **36**, 4175 (2017).

[22] M. Goldman, A. Goldman, and R. S. Sigmond, The corona discharge, its properties and specific uses, Pure. Appl. Chem. **57**, 1353 (1985).

[23] S. Park, U. Cvelbar, W. Choe, and S. Y. Moon, The creation of electric wind due to the electrohydrodynamic force, Nat. Commun. **9**, 371 (2018).

[24] G. Dong, Z. Feng, L. Li, and H. Lu, The effect of electron ambipolar diffusion on the ion current signals in a premixed methane flame, Fuel **256**, 115813 (2019).

[25] B. C. Choi and B. J. Park, A 1D ionic transport model for nonlinear response analysis of a counterflow laminar diffusion flame in DC electric fields, Fuel **233**, 610 (2018).

[26] Y. Ren, W. Cui, and S. Li, Electrodydrodynamic instability of premixed flames under manipulations of dc electric fields, Phys. Rev. E **97**, 013103 (2018).

[27] S. Karnani and D. Dunn-Rankin, Detailed characterization of DC electric field effects on small non-premixed flames, Combust. Flame **162**, 2865 (2015).

[28] V. N. Dashevskii and B. S. Fialkov, Free-oscillation regime of diffusional gas combustion in an electric field focused on the preignition zone, Combust. Explo. Shockwave **29**, 352 (1993).

[29] A. R. D. Farraj, A. M. Al-Naeemy, A. N. Al-Khateeb, and D. C. Kyritsis, Laminar non-premixed counterflow flames manipulation through the application of external direct current fields, J. Energy Eng. **143**, 04017002 (2017).

[30] M. D. Renzo, J. Urzay, P. D. Palma, M. D. de Tullio, and G. Pascazio, The effects of incident electric fields on counterflow diffusion flames, Combust. Flame **193**, 177 (2018).

[31] R. J. Kee, J. A. Miller, G. H. Evans, and G. Dixon-Lewis, A computation model of the structure and extinction of strained, opposed flow, premixed methane-air flames, Int. Symp. Combust. **22**, 1479 (1988).

[32] R. F. Johnson, A. C. VanDine, G. L. Esposito, and H. K. Chelliah, On the axisymmetric counterflow flame simulations: is there an optimal nozzle diameter and separation distance to apply quasi one-dimensional theory? Combust. Sci. Technol. **187**, 37 (2015).

[33] D. G. Park, S. H. Chung, and M. S. Cha, Dynamic responses of counterflow nonpremixed flames to AC electric field, Combust. Flame **198**, 240 (2018).

[34] B. C. Choi, H. K. Kim, and S. H. Chung, Effect of AC electric fields on counterflow diffusion flame of methane, Trans. Korean Soc. Mech. Eng. B **36**, 849 (2012).

[35] M. Kono, K. Iinuma, and S. Kumagai, The effect of dc to 10 MHz electric field on flame luminosity and carbon formation, Proc. Combust. Inst. **18**, 1167 (1981).

[36] M. Kono, F. B. Carleton, A. R. Jones, and F. J. Weinberg, The effect of nonsteady electric fields on sooting flames, Combust. Flame **78**, 357 (1989).

[37] L. Sun, G. Lins, and T. Hammer, Interaction of a low-pressure flat flame with an electric field, in *Proceedings of the European Combustion Meeting* (2005).

[38] A. M. Drews, L. Cademartiri, M. L. Chemama, M. P. Brenner, G. M. Whitesides, and K. J. Bishop, Ac electric fields drive steady flows in flames, Phys. Rev. E **86**, 036314 (2012).

[39] Y. Xiong, D. G. Park, B. J. Lee, S. H. Chung, and M. S. Cha, DC field response of one-dimensional flames using an ionized layer model, Combust. Flame **163**, 317 (2016).

[40] J. S. Townsend, M. A. Dublin, and C. Maxwell, The diffusion of ions into gases, Philos. Trans. A **193**, 129 (1899).

[41] M. Cowie and H. Watts, Diffusion of methane and chloromethanes in air, Can. J. Chem. **49**, 74 (1971).

[42] E. L. Cussler, *Diffusion: Mass Transfer in Fluid Systems*, 2nd ed. (Cambridge University Press, Cambridge, 1997).

[43] S. A. Klein, Engineering Equation Solver (2019), http://fchartsoftware.com/ees/.

[44] M. D. Renzo, G. Pascazio, and J. Urzay, The breakdown of self-similarity in electrified counterflow diffusion flames, Combust. Flame **205**, 231 (2019).

[45] M. Woo, B. C. Choi, and A. F. Ghoniem, Experimental and numerical studies on NOx emission characteristics in laminar non-premixed jet flames of ammonia-containing methane fuel with oxygen/nitrogen oxidizer, Energy **114**, 961 (2016).